Integral equation based modeling of the piezoceramic patch actuators' interaction with an elastic substrate

Evgeny Glushkov[1], **Natalia Glushkova**[1], **Oleg Kvasha**[1] **and Wolfgang Seemann**[2]

[1] Kuban State University, P.O. Box 1581, Krasnodar 350080, Russia
[2] Karlsruhe University, P.O. Box 6380, Kaiserstr. 12, D-76128 Karlsruhe, Germany

Abstract. An integral equation based model for a system of piezoceramic flexible patch actuators bonded to an elastic substrate (layer or half-space) is developed. The rigorous solution to the coupled patch-substrate dynamic contact problem extends the range of model's feasibility far beyond the bounds of conventional models relying on simplified plate, beam or shell equations for the waveguide part. In particular, the proposed approach has provided a possibility to reveal the effect of resonance energy radiation associated with higher modes that would be inaccessible in the context of simplified models. In view of the correct accounting for the actuators' mutual wave interaction via the host medium, the algorithms for selective mode excitation in a layer as well as for body waves directing to required zones in a half-space have been also derived and computer implemented.

PACS numbers: 43.38.Fx, 43.38.Hz, 43.20.Mv, 46.40.Cd, 46.40Ff

Submitted to: *Smart Mater. Struct.*

1. Introduction

Nowadays, piezoceramic smart materials, providing strong mechanical response on an applied electric field, have been gaining wide popularity. Electromechanical systems with piezoceramic actuators and sensors in the form of flexible patches bonded to elastic waveguide structures find application in ultrasonic non-destructive evaluation and structural health monitoring, e.g. of shell structures of aerospace units, in active systems of vibration damping, in precision mechanical positioning gears and ultrasonic surface wave motors, etc. The advantages of piezoceramic patches are their small weight, flexibility, and relatively low cost; therefore, in many cases the piezoceramics replaces traditional electromechanical and piezo-crystal devices.

In the design of piezoceramically based systems an important part is the development of mathematical models adequately describing elastic wave excitation by piezoceramic patches. The traveling elastic waves are generated in the structure by the

contact shear tractions q resulting from longitudinal patch deformation under transverse electric field E_z due to the piezoelectric effect (figure 1). Being bonded to the structure, the patches produce bending strains. Therefore, first mathematical studies were devoted to flexural and longitudinal wave motion of thin-walled structures governed by simplified beam, plate or shell equations [1, 2, 3, 4] (see also surveys in [3, 5, 6]). In these models the actuating force is replaced by a pair of opposite concentrated forces applied at the points of patch edges (pin-force models). To provide the equivalence of their action on the waveguide to the action of a modeled patch, the amplitude of the forces is rigorously derived in terms of both patch and structure material and geometrical characteristics. In some models the inertia effect of the patches as well as 3D geometry are also taken into account (e.g., see [7, 6]).

Such simplified models operate only with the first fundamental (bending and longitudinal) guided wave modes, therefore providing simple, physically clear description of the elastodynamic wave processes in the substructure. However, the area of their application is restricted. They are only valid in a low frequency band, where the characteristic wavelength is much greater than the plate or shell thickness.

There are several reasons of such models' shortage. First, the plate, beam and shell equations are not destined to account for higher Lamb modes excited in layer waveguides at higher frequencies. The more so, they cannot provide surface waves of Rayleigh type. Then, a group work of actuators is modeled by a simple superposition of pin-force moments simulating their action. Hence, they do not take into account mutual influence of system elements on source characteristics that often is necessary for a proper phasing of driving electric fields. To surmount these limitations, one has to use a richer waveguide model (elastic layer, half-space, pack of layers, etc) and to describe strictly the patch-elastic base dynamic interaction.

The latter is achievable using the FEM discretization technique. However, FEM solutions cannot provide a direct insight into the wave structure (e.g., to give at once the source energy distribution among several guided waves excited in a multimode range); in addition, a classical FEM is not applicable to infinite open waveguides for it operates with space-restricted discretization domains. This obstacle is not critical; it may be avoided by introducing special infinite elements (e.g., strip elements proposed in [8]) or using improved hybrid schemes, which combine FEM solutions in limited areas with expansions in terms of guided waves going to infinity [9].

At the same time, there exists a possibility to obtain a physically clear view on the wave structure simultaneously with the same quantitative data like FEM might provide, but without cumbersome stitch procedures. It is accomplishable with the integral equation approach based on the use of exact integral representations of wave fields generated in elastic layered structures by surface tractions or buried forces. Substitution of such integral expressions into the patch-layer contact boundary conditions reduces initial boundary-value problems to integral equations with respect to unknown contact stresses (in our case, to the shear traction q). Semi-analytical solutions of the integral equations enable fast wave field calculations, especially by the use of the residual

technique. The latter yields explicit expansions in terms of guided waves obtained analytically as residues from the integrand's poles. The information about the wave source (patch action) enters into the integral expressions with q, and so, it is retained rigorously in the residual expansions as well.

Thus, the integral equation approach gives a tool for both qualitative and quantitative fast parametrical analysis of piezoceramically based devices and systems. However, its practical implementation requires a thorough preliminary analytical work. Obviously, that is the reason of its comparatively scanty practical employing. As rare examples of works in this field we may cite the papers [10, 11, 12] dealing with a static statement [10], anti-plane shear wave [11] and Rayleigh wave [12] excitation in an elastic half-space. The half-space Green's matrix involved here in the integral representations is much simpler in its form than Green's matrix of an elastic layer or layered structure required for Lamb waves modeling, so that we cannot cite any paper on the patch-layer interaction modeling by the integral equation method, except the previous works of our group [13, 14].

This research was started few years ago relying on the experience in deriving and implementing semi-analytical solutions to the integral equations arising in elastodynamic contact and diffraction problems. There have been developed a variety of methods, such as expansion in terms of splines, orthogonal polynomials and radial basis functions, reduction to infinite algebraic systems, layered element discretization and others (see, e.g., [15, 16] and surveys in [17, 18]). These methods seemed to be quite applicable for the patch-layer interaction analysis; in fact, no critical obstacles had been encountered while extending them onto the problem under consideration.

As was expected, the integral equation based models proved to be a convenient tool for the fine wave phenomena studying. They allowed us, in particular, to reveal the nature of high-mode patch-layer resonance effects [13], as well as to develop the algorithms for the normal mode selective excitation and direction [14]. The prime objective of the present paper is to give a possibly full and consistent explanation of the model developed. Then, the numerical examples illustrating the models' validation and its capability are discussed. Wherever possible, we present other numerical examples than in [13, 14]. In particular, a new comparison with a plate model is carried out in the validation section 3, which is supplemented by examples of boundary condition control and testing against the half-space model from [12]. Besides, new algorithms for body wave directional radiation control are presented in section 5, in addition to the selective mode excitation algorithms developed in [14].

2. Mathematical model

The derivation of Green's matrices and integral representations is based on the application of the Fourier transform with respect to horizontal space coordinates. Therefore, the mathematical technique described below is applicable with any layered or even vertically inhomogeneous (gradient) substructures having only plane horizontal

boundaries and interfaces (piece-wise continuous vertical stratification). It may be not only an elastic half-space or layer but, for example, a pack of layers simulating laminate composite materials. However, for clarity sake, we will give the main idea on the example of a homogeneous elastic layer of finite thickness h, discussing in parallel the peculiarities of model's implementation with other kinds of elastic base, first of all, with an elastic half-space occurring with $h = \infty$.

2.1. Coupled patch-layer boundary-value problem

As a substructure, let us consider a homogeneous isotropic layer of thickness h, occupying the domain $-\infty \le x \le \infty$, $-h \le z \le 0$, with M thin and flexible piezoceramic strip actuators of thickness $h_m, m = 1, 2, ..., M$, bonded to its top surface $z = 0$ (figure 1). The bottom surface $z = -h$ is stress-free, while the longitudinal deformation of the strips in response to a transversal electromagnetic field $E_z e^{-i\omega t}$ causes an unknown shear load $\tau_{xz} = qe^{-i\omega t}$ applied to the stress-free top side $z = 0$ in the disconnected region $\Omega = \cup_m \Omega_m$; $\Omega_m : |x - x_m| \le a_m$ is the contact area of m-th strip. The waveguide is assumed to be in the plane-strain conditions, so the load q generates a 2D in-plane harmonic wave field $\mathbf{u}(x, z)e^{-i\omega t}$, $\mathbf{u} = \{u_x, u_z\}$ being the displacement vector (its complex amplitude). Below, the time-harmonic factor $e^{-i\omega t}$ is conventionally omitted, so that only space dependent complex amplitudes are involved into consideration.

Mathematically, $\mathbf{u}(x, z)$ obeys the Lamé equations

$$(\lambda + \mu)\nabla \mathrm{div}\, \mathbf{u} + \mu \Delta \mathbf{u} + \rho\omega^2 \mathbf{u} = 0 \tag{2.1}$$

and the boundary conditions

$$\boldsymbol{\tau}|_{z=0} = \begin{bmatrix} q \\ 0 \end{bmatrix}, \qquad \boldsymbol{\tau}|_{z=-h} = \begin{bmatrix} 0 \\ 0 \end{bmatrix}. \tag{2.2}$$

Here λ, μ are Lamé constants, ρ is the density, $\boldsymbol{\tau} = \{\tau_{xz}, \sigma_z\}$ is the stress vector at a horizontal surface element. Hereinafter, the vectors are assumed to be vector-columns; to underline this fact their components written in a line are given in braces as distinct from conventional brackets for matrices.

With ideally elastic material properties boundary conditions are to be supplemented by certain radiation conditions assuring the uniqueness. As the radiation condition we use the principle of limiting absorption, which means that the solution for an ideally elastic medium is the limit of the unique solution of the corresponding problem for a medium with attenuation ε as $\varepsilon \to 0$.

The distribution of contact stresses $q(x)$ ought to be found taking into account both the dynamic layer response and the longitudinal strip deformation $\varepsilon_x = \partial v/\partial x$ (here $v(x)$ is an unknown horizontal patch displacement). Therefore, equations of longitudinal wave motion of patches should be also introduced into the mathematical statement. Henceforth, it is convenient to consider q and v as a superposition of contact stresses

$q_m(x)$ and displacements $v_m(x)$ of each strip:

$$q = \sum_{m=1}^{M} q_m, \quad v = \sum_{m=1}^{M} v_m \tag{2.3}$$

where $q_m(x)$ and $v_m(x)$ are extended on the whole axis x by zero:

$$q_m(x) = \begin{cases} q(x), & x \in \Omega_m \\ 0, & x \notin \Omega_m \end{cases}, \quad v_m(x) = \begin{cases} v(x), & x \in \Omega_m \\ 0, & x \notin \Omega_m \end{cases}$$

Due to strips flexibility, we assume that they do not produce vertical contact stresses σ_z and vertical patch displacements do not influence on q. We also assume that the patch thickness $h_m << \lambda$, where λ is a characteristic wavelength in the piezoceramics, and, as a consequence, v is independent of the transverse coordinate z. In addition, the shear strains γ_{xz} are also supposed negligible. The electric field $\mathbf{E} = \{0, E_z\}$ is purely transverse and uniform within each strip ($E_z = \cup_m E_{z,m}$, where $E_{z,m} = |E_{z,m}|e^{i\theta_m}$ are complex constants giving amplitudes $|E_{z,m}|$ and phase shifts θ_m of a driving field E_z interacting with each strip). Under these assumptions, the generalized Hooke's law, which gives a linear matrix relation between the components of the stress and strain tensors and the electrical field vectors $\mathbf{E}$, is reduced to the scalar relationship [10]

$$\sigma_x = \frac{E_m}{1-\nu_m^2}[\varepsilon_x - d_{31,m}(1+\nu_m)E_{z,m}] \tag{2.4}$$

where E_m, ν_m and $d_{31,m}$ are Young's modulus, Poisson's ratio and electromechanical coupling constant of m-th piezoceramic patch.

To derive the equation of motion for patches, let us consider a strip element of length dx, height h_m and width dy (figure 1). The resultant longitudinal force df_x acting on this element is composed of the sum of forces resulted from stresses $-\sigma_x$ and $\sigma_x + d\sigma_x$ at the element's side edges, the force $-q_m dxdy$ caused by the contact tension q_m and the inertia force $\ddot{v}\rho_m h_m dxdy$:

$$df_x = h_m dyd\sigma_x - q_m dydx - \ddot{v}\rho_m h_m dydx \tag{2.5}$$

ρ_m is the material density; $\ddot{v} \equiv \partial^2/\partial t^2(ve^{-i\omega t}) = -\omega^2 v$. Taking into account (2.4), the equilibrium condition $df_x = 0$ is reduced to the equations of patch motion

$$\mathcal{M}_m v_m \equiv \frac{1}{b_m}\left(\frac{d^2 v_m}{dx^2} + \kappa_{0,m}^2 v_m\right) = q_m, \quad x \in \Omega_m, \quad m = 1, 2, ..., M \tag{2.6}$$

where $\kappa_{0,m}^2 = \omega^2 \rho_m h_m b_m$ and $b_m = (1-\nu_m^2)/(h_m E_m)$.

The side faces of strips are stress-free: $\sigma_x(x_m \pm a_m) = 0$; in view of equation (2.4) it yields boundary conditions

$$dv_m/dx|_{x=x_m \mp a_m} = e_m, \quad e_m = d_{31,m}(1+\nu_m)E_{z,m}, \ m = 1, 2, ..., M, \tag{2.7}$$

supplementing equations (2.6).

The equations with respect to wave field $\mathbf{u}$ and patch displacement v are coupled not only by the same stress function q entering in eqs. (2.2) and (2.6), but also by the condition of displacement continuity

$$u_x(x, 0) = v(x), \quad x \in \Omega. \tag{2.8}$$

In the whole, the patch-layer electromechanical interaction is simulated by the solution to the coupled boundary value problem with eqs. (2.1), (2.6) and boundary conditions (2.2), (2.7), and (2.8).

2.2. Integral representations

The geometry of the problem allows us to apply the Fourier transform with respect to the horizontal variable x:

$$\begin{aligned} &\mathcal{F}[\mathbf{u}] \equiv \int\limits_{-\infty}^{\infty} \mathbf{u}(x,z)e^{i\alpha x}dx = \mathbf{U}(\alpha,z) \\ &\mathcal{F}^{-1}[\mathbf{U}] \equiv \tfrac{1}{2\pi}\int\limits_{\Gamma} \mathbf{U}(\alpha,z)e^{-i\alpha x}d\alpha = \mathbf{u}(x,z) \end{aligned} \tag{2.9}$$

Here $\mathcal{F}$ and $\mathcal{F}^{-1}$ are operators of the direct and inverse Fourier transforms, Γ is the integration path going in the complex plane α along the real axis $\operatorname{Im}\alpha = 0$ deviating from it for bypassing real poles and branch points of the integrand $\mathbf{U}$ in accordance with the principle of limiting absorption (figure 2).

In the Fourier-transform domain the Lamé equations (2.1) are reduced to the system of ordinary differential equations (ODE), which may be written in the following matrix form [15]

$$\mathbf{Y}'(\alpha,z) = A(\alpha,z)\mathbf{Y}(\alpha,z) \tag{2.10}$$

Here $\mathbf{Y} = \{U_x, U_x', U_z, U_z'\}$ is a vector-column combined from the components of the transformed displacement vector $\mathbf{U} = \mathcal{F}[\mathbf{u}]$ and its z-derivative $\mathbf{U}'$ (hereinafter, z-derivatives are conventionally marked by a stroke); A is a 4×4 matrix with elements easily derived from (2.1) in an explicit analytical form.

The general solution to this ODE is

$$\mathbf{Y} = \sum_{j=1}^{4} c_j \mathbf{m}_j e^{\gamma_j z} \tag{2.11}$$

where γ_j and $\mathbf{m}_j$ are eigenvalues and associated eigenvectors of matrix A:

$$\gamma_j:\ \det(A-\gamma_j E) = 0 \tag{2.12}$$

$$\mathbf{m}_j:\ (A-\gamma_j E)\mathbf{m}_j = 0 \tag{2.13}$$

whereas c_j are unknown constants to be obtained from the transformed boundary conditions (2.2). The roots of the characteristic equation (2.12) are derived analytically:

$$\gamma_{1,2} = \pm\sigma_1, \gamma_{3,4} = \pm\sigma_2;\ \ \sigma_n = \sqrt{\alpha^2-\kappa_n^2}, n = 1,2,$$

here $\kappa_1 = \omega/v_p$ and $\kappa_2 = \omega/v_s$ are wave numbers of P and S body waves in the elastic volume; $v_p = \sqrt{(\lambda+2\mu)/\rho}$ and $v_s = \sqrt{\mu/\rho}$ are their velocities; the branches of the square roots σ_n in the complex plane α are fixed by the conditions $\operatorname{Re}\sigma_n \geq 0$ and $\operatorname{Im}\sigma_n \leq 0$ as $\alpha \in \Gamma$. Then, the eigenvectors $\mathbf{m}_j$ are also derived from (2.13) in a closed form.

Since a stress vector $\boldsymbol{\tau}$ at an arbitrary surface element fixed by a unit normal $\mathbf{n}$ is connected with the displacement field $\mathbf{u}$ by the stress operator T_n: $\boldsymbol{\tau} = T_n\mathbf{u} \equiv \lambda\mathbf{n}\mathrm{div}\,\mathbf{u} + 2\mu\partial\mathbf{u}/\partial\mathbf{n} + \mu(\mathbf{n}\times\mathrm{rot}\,\mathbf{u})$, in the Fourier transform domain the conditions (2.2) are reduced to the matrix equalities

$$T\,\mathbf{Y}|_{z=0} = \begin{bmatrix} Q \\ 0 \end{bmatrix}, \quad T\,\mathbf{Y}|_{z=-h} = \begin{bmatrix} 0 \\ 0 \end{bmatrix} \tag{2.14}$$

in which

$$T = \begin{bmatrix} 0 & \mu & -i\alpha\mu & 0 \\ -i\alpha\lambda & 0 & 0 & \lambda+2\mu \end{bmatrix}, \quad Q = \mathcal{F}[q].$$

The substitution of the general solution (2.11) into eqs. (2.14) yields the linear algebraic system

$$B\mathbf{c} = \mathbf{Q} \tag{2.15}$$

with respect to the vector of unknown constants $\mathbf{c} = \{c_1, c_2, c_3, c_4\}$; the elements of matrix B are combined from the T and $\mathbf{m}_j$ components, as well as the exponents $e^{\pm\sigma_n h}$, in accordance with the substitution.

In the case under consideration $\mathbf{Q} = \{Q, 0, 0, 0\}$, while, in the general case, $\mathbf{Q} = \mathcal{F}[\mathbf{q}]$, where $\mathbf{q} = \{\mathbf{q}^+, \mathbf{q}^-\}$ includes both loads $\mathbf{q}^+$ and $\mathbf{q}^-$ applied to the surfaces $z = 0$ and $z = -h$, respectively. Consequently, with such general boundary conditions the Fourier transformed solution $\mathbf{U}$ (Fourier symbol of $\mathbf{u}$) may be written in the following form

$$\mathbf{U}(\alpha, z) = K^+(\alpha, z)\mathbf{Q}^+(\alpha) + K^-(\alpha, z)\mathbf{Q}^-(\alpha), \quad -h \le z \le 0 \tag{2.16}$$

where $K^\pm$ are 2×2 matrices, the columns of which are the Fourier symbols of displacements generated in the layer by tangential and vertical point-force loads: $\tau_{xz} = \delta(x)$ for the first column and $\sigma_{zz} = \delta(x)$ for the second one (δ is Dirac's delta-function); these loads are applied to the top or to the bottom surface for K^+ or K^-, respectively; $\mathbf{Q}^\pm = \mathcal{F}[\mathbf{q}^\pm]$. All these solutions have the same general form (2.11), but with the constants c_j obtained from four systems

$$B\,\mathbf{c} = \mathbf{e}_i, \quad i = 1, 2, 3, 4 \tag{2.17}$$

differing from (2.15) and one another in the right hand sides only. Namely, $\mathbf{e}_i$ are unit vectors with the only i-th non-zero component: $\mathbf{e}_1 = \{1, 0, 0, 0\}$ for the first column of K^+, $\mathbf{e}_2 = \{0, 1, 0, 0\}$ for its second column, and so on.

The explicit analytical form of elements of Green's matrices $K^\pm$ may be found, for example, in [13, 18]. However, it is of little practical importance for a computer code implementing, their calculation may rely on algorithms following directly from eqs. (2.11), (2.17). In other words, with each new value of the input parameter α, the values of $K^\pm(\alpha, z)$ elements may be computed in line with (2.11), with c_j being determined numerically from systems (2.17). Such a way of Green's matrices calculation is even better for coding than explicit expressions that often are too cumbersome.

Moreover, only such a way enables practical computer implementation with a multilayered structure. The substitution of general solutions written in the form (2.11)

for each of the sublayers of an N-layered laminate into the external and interface boundary conditions leads to an algebraic system of size $4N$ with respect to the vector of unknown constants $\mathbf{c} = \{\mathbf{c}_1, \mathbf{c}_2, ..., \mathbf{c}_N\}$; here $\mathbf{c}_k$ are vectors of length 4 for the each of sublayers. Since only neighbour vectors $\mathbf{c}_k$ and $\mathbf{c}_{k+1}$ are connected by matrix relations following from the interface stitch conditions, the global matrix B of this system is of block-diagonal structure. Hence, its solution may be organized using certain recurrent matrix algorithms going back to the pioneering algorithms by Haskel, Tompson and Petrashen' (e.g., see review of matrix algorithms in [19]). One more way is to take solutions in each sublayer directly in the form (2.16) with unknown interface stresses $\mathbf{Q}^{\pm}$, which are excluded then using the interface stitch conditions.

In more detail, the algorithms developed for numerically stable Green's matrices calculation are described in [15, 18]. The main thing is that with any stratification the solution is obtained in the form (2.16); hence, as soon as the calculation of matrices $K^{\pm}$ is implemented, the proposed general scheme of the coupled problem solution works disregarding their specific appearance for a stratified substrate under study.

Turning back to the problem in question, since $\mathbf{Q} = \{Q, 0, 0, 0\}$, the wave field $\mathbf{u}$ excited in the layer can be represented via the inverse Fourier transform in the following form:

$$\mathbf{u}(x, z) = \frac{1}{2\pi} \int\limits_{\Gamma} \mathbf{K}_1(\alpha, z) Q(\alpha) e^{-i\alpha x} d\alpha \tag{2.18}$$

where $\mathbf{K}_1$ is the first column of the matrix K^+ for the layer calculated via solving only the first of systems (2.17) with $\mathbf{e}_1$ in the right hand side. With a laminate substructure, $\mathbf{K}_1$ is also the first column of K^+, calculated in that case via the system (2.17) of a larger size proportionate to the number of sublayers, as is explained above.

The simplest appearance of $\mathbf{K}_1$ is obtained for a homogeneous half-space. In the case, $h = \infty$ and the second of conditions (2.2) (at the bottom side) becomes unnecessary. Instead, the radiation conditions as $z \to -\infty$ lead to the requirement $c_2 = c_4 = 0$ in (2.11). Consequently, only components c_1 and c_3 remain to be obtained from system (2.17) reduced to size 2×2. Obviously, with an N-layered pack lying on a half-space this system becomes of size $(4N + 2) \times (4N + 2)$.

2.3. Integral equations

The integral representation (2.18), being substituted into the contact condition (2.8), reduces the initial boundary-value problem to the integro-differential problem

$$\left\{ \begin{array}{ll} \mathcal{K}q & = v \\ \mathcal{M}v & = q \end{array} \right. , \quad x \in \Omega \tag{2.19}$$

with $2M$ pointwise conditions (2.7) imposed on $v(x)$. Here

$$\mathcal{K}q \equiv \sum_m \int\limits_{\Omega_m} k(x - \xi) q_m(\xi) d\xi = \frac{1}{2\pi} \sum_m \int\limits_{\Gamma} K(\alpha) Q_m(\alpha) e^{-i\alpha x} d\alpha \tag{2.20}$$

is the Wiener-Hopf type integral operator with the kernel symbol $K(\alpha) = K_1^{(1)}(\alpha, 0)$ to be the first component of the vector-function $\mathbf{K}_1$ at $z = 0$; while the differential operator $\mathcal{M}v$ generalizes ODEs (2.6).

A natural way of this problem solution is Galerkin's discretization scheme via $v_m(x)$ and $q_m(x)$ expansion in terms of certain basis functions (splines, orthogonal polynomials and so on). Its main advantage is in comparatively simple computer implementation disregarding to specific properties of the substructure (either it is a layered waveguide or a half-space). On the other hand, with an increase of frequency the form of the approximated functions becomes more complicate, which requires supplementing the number of terms, and so enlarges the size of systems and the computational costs.

Another efficient approach relies on the path integral evaluation using the residual technique. With a pure meromorphic kernel symbol $K(\alpha)$ (that is the case with any layered substructure of finite thickness h) it reduces the problem to an infinite algebraic system with regard to unknown coefficients $t_k^{\pm}$ in the wave field expansion in terms of normal modes (see (2.22) below). This method is more difficult in implementation than the Galerkin scheme, for it requires to find previously all real and complex poles ζ_k and zeros z_l of the kernel symbols. On the other hand, it provides higher accuracy and lower computational costs by taking explicitly into account the guided wave structure of the solution, which is obtained in a physically clear analytical form. In other words, the corrugation of the sought-for functions q and v due to spatial oscillation of interface waves in the contact zone is excluded from the approximation and numerical computation, so that only not sensitive to frequency expansion coefficients are to be found. As a result, this approach is of little sensitivity to the frequency increasing. Therefore, this is a basic method that we use for the patch-layer elastodynamic interaction modeling.

Its general scheme in the case of one surface obstacle is given in [16] while the modification for the case under consideration, with several strips bonded to a layer, is presented in [13]. The most detailed description is also available in the deposited paper [20]. Therefore, in the present paper we shall restrict ourselves by the remarks above, considering q and v in the consequent text as known functions obtained in one way or another from the coupled problem (2.19), (2.7).

2.4. Wave fields in the substructures

As soon as $\mathbf{K}_1$ and unknown contact traction q are obtained, eq. (2.18) provides a general possibility for the calculation of the wave field $\mathbf{u}$ excited in the substructure. In view of (2.3), $Q = \sum\limits_m Q_m$ with $Q_m = \mathcal{F}[q_m]$, and the total wave field is representable as a superposition of wave fields $\mathbf{u}_m$ generated independently by each load q_m: $\mathbf{u} = \sum\limits_m \mathbf{u}_m$. The fields $\mathbf{u}_m$ are performed in the same form (2.18) with Q replaced by Q_m.

It is worthy to note that $\mathbf{u}_m$ *are not* the fields generated by solitary strips independently of all other actuators, as is conventionally assumed in simplified models. The mutual wave interaction of actuators via the substructure results in changes in the

contact stresses $q_m(x)$, which may differ considerably from the stress under a single strip. Within the model considered such mutual influence of actuators working in group is strictly taken into account in the integral relationship (2.19) connecting q_m with each other.

Furthermore, with any laminate waveguide of finite thickness $h < \infty$, including, of course, the homogeneous layer under study, the elements of matrices $K^{\pm}(\alpha, z)$ are meromorphic functions of α (i.e. without branch points). In the complex plane α they have a finite number of real poles $\pm\zeta_k, k = 1, 2, ..., N_r$ and an infinite set of complex ones: $\pm\zeta_k, k = N_r + 1, N_r + 2, ...$ These poles are roots of the characteristic equation

$$\Delta(\alpha, \omega) \equiv \det B(\alpha, \omega) = 0 \tag{2.21}$$

where B is the matrix of systems (2.15) and (2.17). The poles appear in pairs, because $\Delta(\alpha, \omega)$ is even with respect to both variables. We assume that poles $+\zeta_k$ are located in the α-plane above the integration path Γ, while $-\zeta_k$ lie below it, and the complex poles are arranged in order of imaginary parts increasing ($|\mathrm{Im}\,\zeta_{k+1}| \geq |\mathrm{Im}\,\zeta_k|$) (figure 2).

This meromorphic property permits to represent each of the fields $\mathbf{u}_m$ excited outside the contact domain Ω_m in terms of normal modes:

$$\mathbf{u}_m(x, z) = \sum_{k=1}^{\infty} t^{\pm}_{m,k} \mathbf{a}^{\pm}_k(z) e^{\pm i\zeta_k(x - x_m \mp a_m)}, \quad x \notin \Omega_m \tag{2.22}$$

Here $t^{\pm}_{m,k} = i\, r_k Q_m(\mp\zeta_k) e^{\pm i\zeta_k(x_m \pm a_m)}$, $r_k = \mathrm{res}\, K(\alpha)|_{\alpha=\zeta_k}$, $\mathbf{a}^{\pm}_k(z) = \mathbf{K}_1(\alpha, z)/K(\alpha)|_{\alpha=\mp\zeta_k}$; the upper and lower signs for each item are taken for $x > \Omega_m$ and $x < \Omega_m$, respectively. The terms corresponding to the real poles ζ_k describe traveling waves going to infinity with phase and group velocities $c_{p,k} = \omega/\zeta_k$ and $c_{g,k} = d\omega/d\zeta_k$, while complex ζ_k yield inhomogeneous exponentially decaying waves.

Representation (2.22) is not valid for the wave field in the contact zone, i.e., if $x \in \Omega_m$, because it is derived under assumption $|x - x_m| > a_m$ that makes the exponential function $e^{-i\alpha x}$ in the integrand (2.18) to be principal. It determines the direction of the contour closing into the upper half-plane $\mathrm{Im}\,\alpha \geq 0$ if $x < x_m - a_m$, and conversely, into the lower half-plane if $x > x_m + a_m$, in accordance with Jordan's lemma.

As $x \in \Omega_m$ ($|x - x_m| < a_m$), the exponentials $e^{i\alpha(x_m \pm a_m)}$ entering into $Q_m(\alpha)$ become the governing ones (see the general structure of Q_m given by eq. (3.7) in [13]). Consequently, the integrand is split into two parts in accordance with the direction of closing (upward for the terms with exponents $e^{i\alpha(x_m + a_m)}$ and downward with $e^{i\alpha(x_m - a_m)}$). By doing so, the eliminable poles of the entire function $Q_m(\alpha)$, induced by zeros z_l of its denominator $K(\alpha) - b_m G_m(\alpha)$ become non-eliminable, while the poles ζ_k of $K(\alpha)$ in (2.18) are, in contrast, getting removed. Therefore, the wave field in the contact zone Ω_m, as well as the contact stress function $q_m(x)$, are expressed in terms of exponents $e^{\pm i z_l x}$. As was expected, the roots z_l of the dispersion equation

$$K(\alpha) - b_m G_m(\alpha) = 0 \tag{2.23}$$

where $G_m = 1/(-\alpha^2 + \kappa^2_{0,m})$ is the Fourier symbol of the fundamental solution to eq. (2.6), are wave numbers of the interface waves excited in the patch-layer composite structure.

As an example, several first real branches of the dispersion curves $\zeta_k(\omega)$ and $z_l(\omega)$ are displayed in figure 3 ($h_m = h/6$). One can see that two first curves $z_1(\omega)$ and $z_2(\omega)$ are practically the same as the curves relating to the fundamental symmetric and antisymmetric modes s_0 and a_0 (poles ζ_1 and ζ_2, respectively). It means that due to patch flexibility and comparatively small thickness its presence does not affect the characteristics of fundamental modes distinctly, whereas the curves of higher modes change visibly.

It is appropriate to mention here that throughout the paper we present numerical results in a dimensionless form fixed by several basic units. For a homogeneous elastic layer we take $l_0 = h$ as the unit of length, $v_0 = v_s$ as the unit of velocity, and $\rho_0 = \rho$ as the unit of material density, where h, v_s and ρ are layer thickness, S-wave velocity and density of layer material. In this case the dimensionless angular frequency $\omega = 2\pi f h/v_s$, where f is a dimensional frequency. With a half-space ($h = \infty$), the unit of length is usually taken so as to keep the same dimensionless size of patches as a layer; e.g., $l_0 = 6h_m$ to be comparable with the examples in figure 3 and below.

Unless otherwise specified, in the numerical examples of this paper we use the following dimensionless input parameters:

Substrate

$v_s = 1$, $\rho = 1$, $h = 1$ (layer) or $h = \infty$ (half-space), $\nu = 0.3$, $E = 2.6$

Actuators

$v_{s,m} = 0.578$, $\rho_m = 0.997$, $h_m = 1/6$, $2a_m = 8.333$, $\nu_m = 0.3$, $E_m = E/3 = 0.867$;

$e_m = 1$.

If a substructure is of infinite thickness (layered half-space), the elements of Green's matrices are already not pure meromorphic because of the branch points $\pm\kappa_n, n = 1, 2$ appearing in the α-plane in addition to the poles (here κ_n are wave numbers of body waves for the underlying half-space; see notations after eqs. (2.11) - (2.13) above). Therefore, after the contour closing, path integrals over cut sides remain as an addition to the sum of residues (2.22). The far-field asymptotics of these integrals yields P and S body waves excited in the underlying half-space (see [15] for details).

In the simplest case of a homogeneous half-space, the far-field wave structure takes the form

$$\mathbf{u}_m = \begin{cases} t^{\pm}_{m,R}\mathbf{a}^{\pm}_R e^{\pm i\zeta_R(x-x_m\mp a_m)} + O(|x|^{-1}), \quad |x| \to \infty,\ z = O(1) \\ \sum\limits_{n=1}^{2} \mathbf{t}^{(n)}_m(\varphi) e^{i\kappa_n R_m}/\sqrt{R_m} + O(R_m^{-3/2}), \quad R_m \to \infty,\ -\pi < \varphi_m < 0 \end{cases} \tag{2.24}$$

Here $\zeta_R = \zeta_1$ is the single real pole (the Rayleigh pole), $t^{\pm}_{m,R}$ and $\mathbf{a}^{\pm}_R$ are of the same form as $t^{\pm}_{m,1}$ and $\mathbf{a}^{\pm}_1$ in (2.22) above. Hence, the first line of eq. (2.24) yields the Rayleigh wave excited by m-th strip, while the second line gives P and S body waves written in the polar coordinates (R_m, φ_m) centered in the middle of the m-th strip: $x - x_m = R_m \cos\varphi_m$, $z = R_m \sin\varphi_m$; the amplitude vectors of these waves

$$\mathbf{t}^{(n)}_m = -\sqrt{\frac{\kappa_n}{2\pi i}} \sin\varphi_m \mathbf{K}_{1,n}(\alpha_n) Q_m(\alpha_n) e^{-i\alpha_n x_m}$$

are derived by the steepest descend method as a contribution of stationary points $\alpha_n = -\kappa_n \cos\varphi_m$; $\mathbf{K}_{1,n} : \mathbf{K}_1(\alpha, z) = \sum\limits_{n=1}^{2} \mathbf{K}_{1,n}(\alpha) e^{\sigma_n z}$.

2.5. Energy representations

A flow of wave energy in a time-harmonic field is specified by the energy density vector $\mathbf{e} = \{e_x, e_z\}$ time-averaged over the period of oscillation $2\pi/\omega$ (Umov-Poynting vector). The total amount of energy E carried by harmonic waves through a surface S (a time-averaged power) is obtained by surface integration

$$E = \int\limits_S e_n dS \tag{2.25}$$

where $e_n = \mathbf{e} \cdot \mathbf{n} = -\frac{\omega}{2}\mathrm{Im}\,(\mathbf{u}, \boldsymbol{\tau}_n)$, $\mathbf{n}$ is the outward unit normal to S at a current point of integration; $\boldsymbol{\tau}_n = T_n\mathbf{u}$ is the stress vector at this point of S, for a 2D in-plane motion $(\mathbf{u}, \boldsymbol{\tau}) = u_x\tau_x^* + u_z\tau_z^*$; hereinafter, an asterisk denotes the complex conjugation.

Specifically, the source energy E_0 coming from the actuators into the substrate can be obtained by integration over the surface $z = 0$. Due to the boundary conditions it takes the form

$$E_0 = \frac{\omega}{2}\mathrm{Im} \int\limits_\Omega v(x) q^*(x) dx = \frac{\omega}{4\pi}\mathrm{Im} \int\limits_\Gamma K(\alpha) Q(\alpha) Q^*(\alpha^*) d\alpha \tag{2.26}$$

For the energy fluxes $E^\pm$ outgoing to infinity through vertical cross-sections $x = \pm x_0$ eq. (2.25) yields

$$E^\pm(x_0) = \mp\frac{\omega}{2} \int\limits_{-h}^{0} (\mathbf{u}(\pm x_0, z), \boldsymbol{\tau}_x(\pm x_0, z)) dz \tag{2.27}$$

where $\boldsymbol{\tau}_x = T_x\mathbf{u} = \{\sigma_{xx}, \tau_{xz}\}$ is the stress vector at an area element with the normal $\mathbf{n} = \{1, 0\}$.

If the substructure is a layer ($h < \infty$), $K(\alpha)$ is real with real α, so that only residues from real poles ζ_k contribute into the imaginary part of the path integral in (2.26):

$$E_0 = \sum_{k=1}^{N_r} (E_k^+ + E_k^-) \tag{2.28}$$

$$E_k^\pm = \frac{\omega}{4}\mathrm{res}\, K(\alpha)|_{\alpha=\zeta_k} |Q(\mp\zeta_k)|^2 = \frac{\omega}{4r_k} \left| \sum_{m=1}^{M} t_{m,k}^\pm e^{\mp i\zeta_k(x_m \pm a_m)} \right|^2$$

Substitution of $\mathbf{u}$, taken in the form of normal mode expansion (2.22), into equality (2.27) leads to the same expressions as appear in (2.28), which confirms the energy conservation law for a layer: $E_0 = E^+ + E^-$. Besides, it means that $E_k^\pm$ are energies carried to infinity to the right and to the left of sources by each of the traveling waves associated with the real poles ζ_k (see (2.22)).

With a homogeneous half-space ($h = \infty$) the presence of branch points κ_n results in $\mathrm{Im}\, K(\alpha) \neq 0$ at $|\alpha| < \kappa_2$, so that instead of (2.28) the representation of source energy takes the following form

$$E_0 = E_R + E_v \tag{2.29}$$

$$E_R = E_R^+ + E_R^-, \quad E_v = \frac{\omega}{4\pi} \int\limits_{-\kappa_2}^{\kappa_2} \operatorname{Im} K(\alpha) |Q(\alpha)|^2 d\alpha$$

here $E_R^{\pm} = E_1^{\pm}$ are contributions of the Rayleigh poles $\pm\zeta_1$ that coincide with the energy outflow to infinity in a horizontal direction calculated by the integration (2.27). The rest of source energy E_v, obviously, outgoes through the "bottom" $z = \text{const}$ being carried by body P and S waves. This is confirmed by the numerical integration over a horizontal plane $|x| < x_0$, $z = \text{const}$ as $z \to -\infty$ or over a cylindrical surface $x = R\cos\varphi$, $z = R\sin\varphi$, $-\pi \le \varphi \le 0$, as $R \to \infty$. In both these cases $\mathbf{u}$ entering in the integrand e_n in (2.25) is taken in the form of body wave asymptotics ((2.24), second line).

Explicit expressions for wave energy fluxes are used further on as objective functions in the algorithms developed for required modes selective excitation and directive radiation.

3. Validation

There are two aspects of the developed model validation. First, we have to make sure that the code yields numerical solutions namely to the boundary-value problem posed in subsection 2.1. Second, we should test it against other existing models estimating the range of their practical capability.

The first task is accomplished by the verification if a calculated wave field $\mathbf{u}$ obeys the governing equations and satisfies the boundary conditions. It should be noted that due to the semi-analytical structure of the solution, it obeys identically equations (2.1) and conditions (2.2) with any q, as soon as Green's matrix $K(\alpha, z)$ is derived correctly. Therefore, the main point here is the control of bonding condition (2.8), that holds if the solution of the coupled problem (2.19) is correct.

Examples of such tests at various frequencies ω are given in figure 4 for two patches of above selected parameters centered on the layer at $x_{1,2} = \pm 8.333$ and actuated with the phase shift $\theta = \pi/2$ ($e_1 = 1, e_2 = i$). One can see that even at high frequencies, when the form of contact displacements becomes very complicated, $u_x(x, 0)$ calculated via (2.1) coincides with $v(x)$ very well.

In addition to the boundary condition checking up, the energy conservation equalities as well as stitching of asymptotics (2.22), (2.24) with the near field integral representation (2.18) are also used as a current control.

As for comparisons with other integral equation based models, figure 5 presents plots taken from [12] (solid lines for the results obtained by the method developed in that paper and round circles for FEM results) being superimposed on our results given by dots (both results are in the unified dimensionless form). The left subplot is for the contact stress $q(x)$ under the right half of a single strip of semi-width $a = 1$ bonded to an elastic half-plane ($h = \infty$); the right subplot is for the distribution of shear stresses τ_{xz} produced by two actuators in the substrate at the depth $z = -0.5$.

In the units of the present paper the dimensionless input parameters of actuators

differing from the default values are as follows: $a_m = 1, h_m = 1/20, x_1 = 0, x_2 = 3$, $E_m = 8.168$ and $e_m = 0.111$. The latter is to obtain the same normalization as in [12]. One can see, there is no visible difference among the solutions to eq. (2.19) (dots) and to the integral equation [12] (solid lines), while FEM results slightly deviate from them.

This comparison is made for a quasistatic state ($\omega \to 0$). With moderate dimensionless frequencies $\omega > 0$ a reasonable agreement of the results also holds, whereas, as ω increases, the discrepancy becomes increasingly large, up to a considerable difference at $\omega > 10$, when the contact stress gets heavily waved. The reason of this discrepancy is, obviously, in the freezing in [12] the number of Chebyshev polynomials (terms of discretization) used in quasistatic for the remainder of study at all frequencies. Whereas, as is underlined in subsection 2.3 above, to keep the accuracy with an increasing complicated form of contact stresses, the number of basis functions in Galerkin's scheme has to be increased in parallel with the frequency growth. The second approach to the contact problem solution developed in [16, 13] is based on the explicit accounting for the interface waves in the contact zone, so it is much less sensitive to a frequency growth.

For the layer model ($h = 1$) comparisons have been carried out against simplified beam [21] and plate [13] models approximating the layer behaviour at low frequencies $\omega << 1$. As was expected, those results agreed well in the low-frequency band $\omega < 0.1$ while they were quite different for $\omega > 1$ even in the subrange $1 < \omega < 3.14$, where only two fundamental (bending and longitudinal) modes exist in both layer and plate waveguides (see figure 3).

Those comparisons were made for the vertical displacement w of the middle plate or beam surface governed by the bending wave equation

$$\frac{d^4 w}{dx^4} - \xi_1^4 w = 0 \tag{3.1}$$

As a continuation, figures 6 - 7 present similar test comparisons for the horizontal displacement $u_x(x, 0)$. In the context of Kirchhoff's plate theory it depends on both bending and longitudinal waves:

$$u_x(x, z) = u(x) - (z + h/2)w^{'}(x) \tag{3.2}$$

here $w(x)$ is as above and $u(x)$ is the axial displacement of the middle plate surface $z = -h/2$ governed by the equation

$$\frac{d^2 u}{dx^2} + \xi_2^2 u = 0 \tag{3.3}$$

In these equations $\xi_1^4 = \rho\omega^2 h/D$ and $\xi_2^2 = \rho\omega^2 h/B$ are wave numbers of the bending and longitudinal waves in Kirchhoff's plates (in figure 3 they are depicted by chain lines); $D = Eh^3/12(1-\nu^2)$ and $B = Eh/(1-\nu^2)$; E and ν are Young's modulus and Poisson's ratio of the plate material.

In accordance with the pin-force models [2] the action of actuators on the plate is simulated by pairs of antiphase forces $\mp F_m$ applied at the end points of strips

$x = x_m \mp a_m$. They are accounted for in the following point-wise boundary conditions imposed on u and w in the points of discontinuity of their derivatives:

$$\begin{aligned} &u^{'}(x_m \mp a_m - 0) - u^{'}(x_m \mp a_m + 0) = \mp F_m/B, \\ &w^{''}(x_m \mp a_m - 0) - w^{''}(x_m \mp a_m + 0) = \pm M_m/D, \quad m = 1, 2, ..., M \end{aligned} \tag{3.4}$$

here $M_m = F_m h/2$ is the magnitude of the point moments associated with the force F_m. Additional boundary conditions required for fixing all constants of the general solutions to the ODEs (3.1) and (3.2) on $2M + 1$ interval, into which these points divide the axis x, are the requirements of continuity for $u(x)$, $w(x)$, $w^{'}(x)$ and $w^{'''}(x)$ at the same strip edge points $x_m \mp a_m$, as well as the radiation conditions at $x \to \pm\infty$ (see also [21]).

The specific values of the point forces F_m may be derived by different ways (e.g., see the survey in [3]). Following [2], we arrived at $F_m = 12e_m D/h^2(4 + \psi_m)$, where $\psi_m = Eh(1-\nu_m^2)/E_m h_m(1-\nu^2)$. Figure 6 gives frequency dependences of the amplitude of horizontal displacements $u_x(x, 0)$ at the surface of the layer (solid lines) and the plate (dashed lines) computed using eqs. (2.18) and (3.2), respectively, at the point $x = 1$ lying between two actuators centered at $x_{1,2} = \mp 2a_m, m = 1, 2$ (upper subplot), and at the point $x = 50$, far away from the sources (lower subplot); the actuators are charged in phase: $e_1 = e_2 = 1$. For comparability with the previous examples for $w(x)$, the patch and plate properties are taken the same as in [13, 21] (see the input parameters in subsection 2.4).

Similarly to those examples, one can see very good agreement in the band $\omega < 0.1$, and different behaviour after $\omega = 3.14$, when the higher modes appear in the layer in addition to the pair of fundamental ones. Certain (non-crucial) difference in an intermediate range (approximately from $\omega = 0.1$ to $\omega = 0.5$) is because the quasistatic approximation used for the pin forces F_m does not take into account the inertia properties of the patch-plate composite. In addition, at higher frequencies the curves of plate fundamental modes ξ_1 and ξ_2 deviate from those for the layer or patch-layer waveguide. The deviation of ξ_1 from the a_0-mode curve is well-visible for $\omega > 0.5$ in figure 3, while ξ_2 differs considerably from the s_0-mode curve only after $\omega > 3$ where curves ζ_2 and z_2 make a turn.

The plots of figure 7 confirm that at low frequencies $\omega < 0.1$ the plate model provides a correct spatial displacement distribution as well.

Thus, from these examples one can conclude that, first, the capability of conventional simplified models are limited by a rather narrow low-frequency band (in the example considered $\omega < 0.1$ or $\lambda_s > 20\pi h$, where $\lambda_s = v_s/f$ is the S-wave length in the plate). Second, the developed layer model, based on the coupled contact problem solution, extends the capability of computer simulation far away beyond those bounds. In particular, it takes into account higher modes that are unachievable in principle with plate, shell or beam waveguide models. Indeed, the numerical analysis carried out for higher frequencies has revealed some new effects controlled by higher modes, such as the resonance of wave energy radiation described in the next section.

4. Resonance properties of wave energy radiation by a piezoceramic strip actuator

4.1. Plate and layer models

With fixed material and electric field parameters the energy E_0 (2.26), supplied by a single strip, depends only on frequency ω and strip width $2a$. The dependencies $E_0(a)$ with $\omega = \text{const}$ are featured by noticeable periodicity due to alternate composition of waves coming from strip edges in phase and anti-phase. Most clearly the mechanism of this effect is seen in a low-frequency band, where a pin-force approximation for the strip action is valid.

Since the point forces F_m and moments M_m, replacing the strip action, operate in antiphase (see eq. (3.4)), the excited waves are composed in phase when the distance between the edges $2a$ is equal to a half-integer number of their wavelengths λ (figure 8):

$$2a = \lambda(n + 1/2), \quad n = 0, 1, 2, ...$$

For bending ($m = 1$) and longitudinal ($m = 2$) modes the wave length $\lambda = 2\pi/\xi_m$ (ξ_m are introduced after (3.3)), therefore, strip sizes a_n, providing maximal amplitude of one of the excited plate modes, are determined by the simple formula

$$a_n = \pi(n + 1/2)/\xi_m, \quad n = 0, 1, 2, ...; \quad m = 1, 2 \tag{4.1}$$

However, in a layer waveguide these simple relations become inapplicable as soon as ξ_m differs from the wave number z_l of the related interface fundamental mode in the patch-layer composite. Obviously, in this case ξ_m in (4.1) must be replaced by z_l.

Indeed, such values a_n shown in the subplots b) and c) of figure 9 by vertical lines coincide well with the maxima of the each mode contribution $E_k(a)$ into the source energy $E_0 = E_1 + E_2$; $E_0(a)$ is given in the upper subplot a); here $\omega = 1$. Values a_n obtained using the formulas (4.1) of plate theory, would yield differing values a_n being unmatched at this frequency with the E_m maxima. Even more so, they would be incorrect at higher frequencies.

Numerical analysis has shown that for $\omega > 3$, as the rule, only one of the wave numbers z_l determines resonance sizes $a_n = \pi(n + 1/2)/z_l$, $n = 0, 1, 2...$ while the others do not contribute noticeably into the $E_0(a)$ dependencies. It is a striking fact, that fundamental modes (both s_0 and a_0) do not occur among such principal modes as $\omega > 3$, where it may be only one of higher modes. In figure 3 such principal sections of dispersion branches z_l are marked by circles ($l = 3$ for $2.7 < \omega < 8.5$, $l = 4$ for $8.5 < \omega < 14$, $l = 5$ for $\omega > 15$ and so on). It is interesting that these sections are aligned in a single line going alongside of the straight line ξ_2 for the wave number of plate dispersionless longitudinal mode (chain line). The most close, however, this line is to the $\operatorname{Re} z_2$ line for the coated half-space (see figure 11 below).

The values of resonance semi-widths a_n, obtained for specified ω by substituting z_l from such marked curves into the expression (4.1) instead of ξ_m, are also shown in subplots d), e) and f) of figure 9 by vertical lines. As can be seen, they match

with the points of maxima of the total source energy $E_0(a)$ very well. Hence, these values a_n may be referred to as points of *strip width resonance* at a fixed frequency. The proximity of principal z_l (marked in figure 3 by circles) to ξ_2 hints at the layer longitudinal displacements to be the determinating factor of the strip width resonance.

In closing, we should remark that this rule of principal branches does not hold so neatly in narrow transient frequency bands occurring usually in the vicinity of outlet points of new branches $z_l(\omega)$ (e.g., for $2.7 < \omega < 3.2$).

4.2. Elastic half-space

Numerical analysis shows that energy radiation into a half-space substrate is also featured by strip width resonance (figure 10). At that, with the frequency increasing, the $E_0(a)$ plots become very similar to those for the layer (e.g., compare subplots f) of figures 9 and 10). From the physical point of view this is quite explainable by the growth of relative thickness h/λ (λ is a wavelength) as ω increases, so that at $\omega >> 1$ the layer works as a bottomless substrate. On the other hand, the wave structure in a half-space is quite different from the normal mode superposition peculiar to a layer. There is only one Rayleigh pole ζ_R and so, only one traveling interface wave in the contact zone specified by the single real zero z_1 (figure 11). Besides, there are two body waves with the wave numbers $\kappa_n, n = 1, 2$ that also contribute as $E_v(a)$ in the source energy radiation to infinity (see (2.29)). With a half-space the variety of decaying inhomogeneous waves associated with complex branches z_l also degenerates in a sole decaying interface mode related to a sole complex root z_2 of eq. (2.23). Similarly to z_1 the dependence of $\operatorname{Re} z_2$ on ω also looks in figure 11 like linear (almost dispersionless phase velocity $c_2 = \operatorname{Re} z_2/\omega$), while the attenuation characteristics $\operatorname{Im} z_2(\omega)$ changes irregularly down to zero at a single point near $\omega \approx 10.65$ (the corresponding real value of z_2 is marked in figure 11 by a circle).

The vertical lines in subplots 10b and 10c relate to the resonance values a_n calculated by (4.1) replacing ξ_m by z_1 and $\operatorname{Re} z_2$, respectively. The resonance maxima of the Rayleigh part of source power $E_R(a)$ are well-described at any ω by those a_n obtained using z_1, while the calculated through $\operatorname{Re} z_2$ values a_n approach to the $E_v(a)$ points of maxima as ω grows up. At that, the contribution of E_v into E_0 becomes principal, hence, at higher frequencies a_n calculated through $\operatorname{Re} z_2$ determine the resonance maxima of $E_0(a)$ as well (subplots 10d - 10f).

The coincidence of these points with those obtained in the context of layer model (figure 9, d) - f)) is elucidated by the fact that the principal sections of branches in figure 3 are aligned in the line going near the line $\operatorname{Re} z_2(\omega)$ of figure 11.

5. Selective mode excitation

Application of normal modes for ultrasonic inspection of plate-like structures generates a need to operate with a single traveling mode over a limited frequency range [22]. With

two patch actuators bonded to opposite sides of a plate, the fundamental s_0 and a_0 modes may by excited separately by applying the driving electric fields $E_{z,m}$ in phase or antiphase. However, in many practically important situations one side of the inspected structure is inaccessible for actuators' bonding (e.g., pipes, tank walls, some parts of frames of chemical plants, engines, aircrafts and so on). All the more, so simple phasing is not enough for the higher modes' selective exciting.

With a set of patch actuators bonded only to one side of a waveguide the problem of required modes excitation and their directional radiation may be also solved by a proper selection of driving fields $E_{z,m}$. The proposed analytically based approach provides a possibility for a strict calculation of such optimal driving parameters. A short communication about the algorithm of selective mode excitation developed in the context of the layer model has appeared in [14]. In the present section we give its more detailed description extending it on the case of a half-plane substrate, that is not only for surface traveling waves, but for the body wave directional radiation into the host medium, too.

5.1. Elastic layer

In the model considered the generalized driving parameters are $e_m = |e_m|e^{i\theta_m}$ introduced in eq. (2.7). With fixed geometry, frequency and material properties only a set of e_m determines the contact stresses q_m, which, being a surface load applied to the substructure, provide then the wave field of general form (2.18) or, specifically for the layer, the normal mode fields (2.22).

Let us split up q_m furthermore, representing them in the form

$$q_m(x) = \sum_{j=1}^{M} e_j q_{m,j}(x), \quad m = 1, 2, ..., M \tag{5.1}$$

Here $q_{m,j}$ are solutions to the integro-differential eq. (2.19) with the boundary conditions

$$dv_{m,j}/dx|_{x=x_m \mp a_m} = \delta_{mj}, \quad m = 1, 2, ..., M \tag{5.2}$$

instead of (2.7), $\delta_{mj} = \begin{cases} 1, & m = j \\ 0, & m \neq j \end{cases}$ is Kroneker's delta, $v_{m,j} : v_m = \sum\limits_j e_j v_{m,j}$.

In other words, the functions

$$q^{(j)} = \sum_m q_{m,j}, \quad v^{(j)} = \sum_m v_{m,j} \tag{5.3}$$

are contact stresses and patch displacements in the case, when a (generalized) unit electric field $e_j = 1$ is applied only to the j-th actuator with zero voltage at all others ($e_m \equiv 0$ as $m \neq j$). These functions are a kind of characteristic (Green's) functions of a piezo-ceramic transducer simulated by the patch-layer model under consideration, since with any vector of driving parameters $\mathbf{e} = \{e_1, e_2, ..., e_m\}$ the resulting characteristics can be expressed in terms of these basis functions:

$$q = \sum_j e_j q^{(j)}, \quad v = \sum_j e_j v^{(j)}, \quad \mathbf{u} = \sum_j e_j \mathbf{u}^{(j)} \tag{5.4}$$

It is worthy to note that elementary functions $q_{m,j}$ and $v_{m,j}$, being solutions to the coupled problem with M strips, also take strictly into account the mutual strip influence due to wave interaction through the substrate.

In view of q splitting (5.4) the related wave fields $\mathbf{u}_m$ can also be expanded in terms of basic fields $\mathbf{u}_m^{(j)}$ excited by basic loads $q_{m,j}$, just as the each normal mode field in (2.22):

$$\mathbf{u}_m = \sum_j e_j \mathbf{u}_m^{(j)} = \sum_j e_j \sum_k \mathbf{u}_{m,k}^{(j)} \tag{5.5}$$

$$\mathbf{u}_{m,k}^{(j)}(x,z) = t_{m,kj}^{\pm}\mathbf{a}_k^{\pm}(z)e^{\pm\zeta_k(x-x_m\mp a_m)}, \quad x \notin \Omega_m$$

$t_{m,kj}^{\pm}$ is of the same form as $t_{m,k}^{\pm}$ in (2.22) replacing Q_m by $Q_{m,j} = \mathcal{F}[q_{m,j}]$. Consequently, in (2.28), the energy of k-th mode $E_k^{\pm}$ is representable as the quadratic form

$$E_k^{\pm} = \sum_i^M \sum_j^M e_i e_j^* (u_{k,i}^{\pm}, u_{k,j}^{\pm}) = (A_k^{\pm}\mathbf{e}, \mathbf{e}) \tag{5.6}$$

where, in line with (2.28), $u_{k,j}^{\pm} = \sqrt{\frac{\omega}{4r_k}} \sum\limits_m t_{m,kj}^{\pm} e^{\mp i\zeta_k(x_m \pm a_m)}$ are combined from the terms related to the first components of vectors $\mathbf{u}_{m,k}^{(j)}$ for $x > \Omega$ and $x < \Omega$, respectively; $A_k^{\pm}$ are the $M \times M$ Hermitian matrices with elements $a_{ij} = (u_{k,i}^{\pm}, u_{k,j}^{\pm}) = a_{ji}^*$ (the inner product assumes conventionally the second factor to be complex conjugated; the same as in $(A_k^{\pm}\mathbf{e}, \mathbf{e})$). Similarly to the basic fields $\mathbf{u}^{(j)}$, the matrices $A_k^{\pm}(\omega)$ are independent of the driving electric fields defining a potential possibility of k-th mode excitation by the specified transducer. The maximal and minimal values of the form (5.6) on a compact set of vectors $\mathbf{e}$ bounded in accordance with some natural practical limitations on the driving parameters (e.g., $|e_j| <$ const or $||\mathbf{e}|| =$ const) relate, obviously, to maximally and minimally possible energy of k-th traveling wave radiated to plus or minus infinity. Thus, the problem of required modes excitation is reduced to the optimization problem with an objective function combined from the quadratic forms (5.6).

In the general case, it is the function

$$\nu(\mathbf{e}) = (A\mathbf{e}, \mathbf{e})/(B\mathbf{e}, \mathbf{e}) \tag{5.7}$$

where $A = \sum\limits_{j=1}^{M_1^+} A_{k_j}^+ + \sum\limits_{j=1}^{M_1^-} A_{l_j}^-$ and $B = \sum\limits_{j=1}^{M_2^+} A_{m_j}^+ + \sum\limits_{j=1}^{M_2^-} A_{n_j}^-$; $k_1, ..., k_{M_1^+}$ and $l_1, ..., l_{M_1^-}$ are numbers of modes to be maximized in the right and left directions of radiation, respectively, while $m_1, ..., m_{M_2^+}$ and $n_1, ..., n_{M_2^-}$ are numbers of modes to be suppressed.

Extremal points of $\nu(\mathbf{e})$ satisfy the extremum conditions:

$$\frac{\partial \nu(\mathbf{e})}{\partial e_j} = 0, \ j = 1, \ldots, M \tag{5.8}$$

which lead to the following nonlinear system

$$(A - \nu B)\mathbf{e} = 0 \tag{5.9}$$

with respect to the vector of unknown parameters $\mathbf{e}$. If the matrix B is not singular ($\det B \neq 0$), the latter expression can be rewritten as

$$R\mathbf{e} - \nu\mathbf{e} = 0, \ R = B^{-1}A, \tag{5.10}$$

and the problem is reduced to the searching for the eigenvector $\mathbf{e}_S$ of matrix R corresponding to its maximal eigenvalue λ_S: $R\mathbf{e}_s = \lambda\mathbf{e}_s$. In such a case $A\mathbf{e}_s = \lambda_s B\mathbf{e}_s$, hence $\nu(\mathbf{e}_s) = \lambda_s$ and eq. (5.10) holds identically.

If matrix B is singular ($\det B = 0$), then its eigenvector $\mathbf{e}_0$ associated with its eigenvalue $\lambda_0 = 0$ being taken as $\mathbf{e}$ provides the full damping of the undesirable radiation: $(B\mathbf{e}_0, \mathbf{e}_0) = 0$. In the event of several eigenvectors $\mathbf{e}_0^{(i)}$ associated with $\lambda_0 = 0$ the vector $\mathbf{e}_s$ maximizing the form $(A\mathbf{e}, \mathbf{e})$ is, obviously, to be searched for in the linear span of these vectors $\mathbf{e}_0^{(i)}$.

Let us derive sufficient conditions making matrix B singular, i.e., the conditions of secure suppression of undesirable modes. Since its elements

$$b_{ij} = \sum_{k=1}^{M_2^+}(u^+_{m_k,i}, u^+_{m_k,j}) + \sum_{k=1}^{M_2^-}(u^-_{n_k,i}, u^-_{n_k,j}) \equiv (\mathbf{w}_i, \mathbf{w}_j)$$

may be treated as inner products of vectors $\mathbf{w}_i = \{u^+_{m_1,i}, ..., u^+_{m_{M_2^+},i}, u^-_{n_1,i}, ..., u^-_{n_{M_2^-},i}\}$, $i = 1, 2, ..., M$, $\det B$ is a gramian of M vectors $\mathbf{w}_i$ of length $M_2 = M_2^+ + M_2^-$. If $M > M_2$, the system of vectors $\mathbf{w}_i$ is linearly dependent, hence $\det B \equiv 0$. If $M \le M_2$, then, in general, $\det B \neq 0$. In other words, M sources are enough to suppress $N < M$ traveling modes completely (at that, the modes $\mathbf{u}_k^{\pm}$ traveling to plus and minus infinity are counted for as two different modes). All one has to do is to fix the driving parameters so that they would meet the condition $B\mathbf{e} = 0$, i.e., to be the eigenvector of B associated with $\lambda_0 = 0$.

For example, to generate a single fundamental mode (s_0 or a_0) in the two-mode range $0 < \omega < 3.14$ that is emitted only in one direction (e.g., to the right of actuators), it is quite enough to use four patches for suppressing the energy of three unnecessary modes: $E_1^- = E_2^- = E_2^+ = 0$ or $E_1^- = E_2^- = E_1^+ = 0$ for the radiation s_0 wave mode $\mathbf{u}_1^+$ or a_0 mode $\mathbf{u}_2^+$, respectively. The plots of surface horizontal displacements $u(x) = u_x(x, 0)$ (both $\mathrm{Re}\, u$ and $\mathrm{Im}\, u$) calculated with driving vectors $\mathbf{e}$ providing such suppressions are depicted in the subplots a) and b) of figure 12 (hereinafter, $\mathbf{e}$ is normalized, so that $|\mathbf{e}| = 1$).

These two examples are for $\omega = 2$ and patches of semi-width $a_m = 1$. As evident from the plots, there is no any backward radiation to the left while to the right of the actuated zone Ω the displacements quickly become of pure sinusoidal form with the spatial periods $2\pi/\zeta_1$ (figure 12a) and $2\pi/\zeta_2$ (figure 12b)). The third subplot 12c illustrates a possibility to generate a so-called backward mode featured by the opposite phase and group velocities ($\mathbf{u}_5$ with $c_{p,5} < 0$ and $c_{g,5} > 0$ at $\omega = 5.5$ in the case). Since there may exist five modes associated with poles ζ_k at this frequency (figure 3), it requires five actuators to suppress four of them at the right side of actuators: $E_k^+ = 0, k = 1, 2, 3, 4$ (the left direction takes no notice in this example).

5.2. Elastic half-space

Since surface Rayleigh waves excited in a half-space are represented in the form (2.24) (first line) by a similar way to the Lamb modes (2.22), the control of their radiation is just a special case of the algorithm described above. In the mean time, the control of body wave radiation ((2.24), second line) leads to a slightly different optimization problem. Though the objective function $\nu(\mathbf{e})$ remains of the same general form (5.7) (it was introduced as far back as in [15] for a similar optimization problem for a group of seismic vibrators), the specific representation of matrices A and B is different. Instead of mode suppression and maximization the main interest in operation with body waves is a control of radiation directivity into the medium.

Let the required direction be an angular sector $\varphi_1 \le \varphi \le \varphi_2$ in the polar coordinates $x = R\cos\varphi$, $z = R\sin\varphi$, $R = \sqrt{x^2 + z^2}$, $-\pi < \varphi < 0$, while in the remaining directions $-\pi < \varphi < \varphi_1$ and $\varphi_2 < \varphi < 0$ the radiation has to be minimized.

It seems natural to introduce the goal function as a ratio of body wave energy flux $E_{v,1}$ through the part of cylindrical surface $\varphi_1 < \varphi < \varphi_2$, $R >> 1$, to the energy flux $E_{v,2}$ through the residual part of this surface:

$$\nu(\mathbf{e}) = E_{v,1}/E_{v,2} \tag{5.11}$$

In accordance with the general representation (2.25)

$$E_{v,1} = \int\limits_{\varphi_1}^{\varphi_2} e_v(R,\varphi) R d\varphi + O(R^{-1}), \quad R \to \infty \tag{5.12}$$

where the power density e_v is calculated retaining only the main terms of the body wave asymptotics (2.24); $E_{v,2}$ is of the same form except the interval of integration ($[-\pi, \varphi_1] \cup [\varphi_2, 0]$ instead of $[\varphi_1, \varphi_2]$). In a homogeneous medium e_v splits into the P and S wave power density [15]:

$$e_v = e_p + e_s, \qquad e_p = \frac{\omega}{2}\kappa_1(\lambda + 2\mu)|u_p|^2, \quad e_s = \frac{\omega}{2}\kappa_2\mu|u_s|^2 \tag{5.13}$$

where u_p and u_s are amplitudes of the first ($n = 1$) and second ($n = 2$) terms of the body wave asymptotics (2.24) of the total field $\sum\limits_m \mathbf{u}_m$ (in fact, they are displacement projections on the radial and transversal directions $\mathbf{n}_p = \{\cos\varphi, \sin\varphi\}$ and $\mathbf{n}_s = \{-\sin\varphi, \cos\varphi\}$, respectively).

Much as above, the body wave asymptotics is also split up in terms of basic fields $\mathbf{u}^{(j)}$ related to unit driving parameters $e_m = \delta_{mj}$ that paves the way to the reduction of the goal function (5.11) to the ratio of quadratic forms $E_{v,1} = (A\mathbf{e}, \mathbf{e})$ and $E_{v,2} = (B\mathbf{e}, \mathbf{e})$. Namely, those representations follow from the expressions for displacement amplitudes in (5.13):

$$|u_p(\varphi)|^2 = |\sum_j e_j \mathbf{t}_j^{(1)}(\varphi)|^2/R, \quad |u_s(\varphi)|^2 = |\sum_j e_j \mathbf{t}_j^{(2)}(\varphi)|^2/R \tag{5.14}$$

where $\mathbf{t}_j^{(n)} = \sum\limits_m \mathbf{t}_{j,m}^{(n)}$, $n = 1, 2$; $\mathbf{t}_{j,m}^{(n)}$ are of the same form as $\mathbf{t}_m^{(n)}$ in (2.24) except Q_m being replaced by $Q_{m,j}$.

Elements a_{ij} and b_{ij} of matrices A and B are obtained by the integration of corresponding expressions over the respective intervals φ; e.g.,

$$a_{ij} = a_{ij}^p + a_{ij}^s$$

$$a_{ij}^p = \frac{\omega}{2}(\lambda + 2\mu)\kappa_1 \int_{\varphi_1}^{\varphi_2} (\mathbf{t}_i^{(1)}(\varphi), \mathbf{t}_j^{(1)}(\varphi)) d\varphi$$

and so on.

Often, only one kind of waves (either P or S) is necessary to control. In such a case only the corresponding terms (a_{ij}^p or a_{ij}^s) are retained in the goal functions. The further calculations (searching for the maximizing eigenvectors $\mathbf{e}_s$) is as before.

We should remark that in contrast to traveling modes associated with a discrete spectrum of the problem (poles ζ_k), the body waves result from the continuous spectrums $0 \le \alpha \le \kappa_n$. Therefore, unlike to normal modes, they cannot be suppressed completely using a finite number of actuators.

The capability to control the body wave radiation in a given direction is illustrated by polar patterns in figure 13. They depict the amplitude factors $|u_p|\sqrt{R}$ and $|u_s|\sqrt{R}$ defined in eq. (5.14) versus the polar angle φ for P (left subplots a)) and S (right subplots b)) for waves generated by ten actuators of size $a_m = 1$ spaced uniformly on the surface of the half-space from $x_1 = -14$ to $x_{10} = 14$. The angular domains $[\varphi_1, \varphi_2]$, in which it was required to maximize the amplitude of generated P and S waves, are marked by bold arcs on the lower semi-circles. As can be seen from these diagrams, the proposed method assures a directional scanning of the substructure by elastic body waves.

6. Concluding remarks

The developed theoretical model for elastic waves excitation by flexible patch actuators bonded to a host medium (2D in-plane motion) has proved its high feasibility in catching fine wave phenomena unattainable with conventional simplified engineering approaches. Among them there is a possibility of operating with higher modes in a multi-mode frequency range, the selective excitation of required Lamb modes and the control of body waves directive radiation into an elastic half-space. The high level of selectivity and directivity provided by the proposed model as well as novel patch-layer resonance effects are illustrated by the numerical examples.

7. Acknowledgements

This work is supported by the grant of the INTAS co-operative project No 05-100008-7979 and by the Russian Foundation for Basic Research (RFBR) grants.

References

[1] Crawley E F and de Luis J 1987 Use of piezoelectric actuators as elements of intelligent structures *AIAA J.* **25** 1373–85

[2] Chaundhry Z and Rogers C A 1994 The pin-force model revisited *J. Intell. Mater. Syst. Struct.* **5** 347–54

[3] Banks H T Smith R C and Wang Yun 1995 The modelling of piezoceramic patch interactions with shells, plates and beams *Q. Appl. Math.* **LIII** 353–81

[4] Seemann W 1996 A linear ultrasonic traveling wave motor of the ring type *Smart Mater. Struct.* **5** 361–8

[5] Giurgiutiu V and Zagrai A N 2000 Characterization of piezoelectric wafer active sensors *J. Intell. Mater. Syst. Struct.* **11** 959–75

[6] Raghavan A and Cesnik C E S 2005 Finite-dimensional piezoelectric transducer modeling for guided wave based structural health monitoring *Smart Mater. Struct.* **14** 1448–61

[7] Liang C, Sun F P and Rogers C A 1994 An impedance method for dynamic analysis of active material systems *J. Vibr. Acoust. (Trans. ASME)* **116** 120–8

[8] Liu G R 2002 A combined finite element/strip element method for analyzing elastic wave scattering by cracks and inclusions in laminates *Comp. Mech.* **28** 76–81

[9] Moulin E, Assaad J and Delebarre C 2000 Modeling of Lamb waves generated by integrated transducers in composite plates using a coupled finite element-normal modes expansion method *J. Acoust. Soc. Am.* **107** 87–94

[10] Seemann W 1997 Stresses in a thin piezoelectric element bonded to a half-space *Appl. Mech. Rev.* **50** 204–9

[11] Zhang B, Boström A and Niklasson A J 2004 Antiplane shear waves from a piezoelectric strip actuator: exact versus effective boundary condition solutions *Smart Mater. Struct.* **13** 161–8

[12] Wang X D and Huang G L 2001 Wave propagation in electromechanical structures: induced by surface-bonded piezoelectric actuators *J. Intell. Mater. Syst. Struct.* **12** 105–15

[13] Glushkov E V, Glushkova N V, Seemann W and Kvasha O V 2006 Elastic wave excitation in a layer by piezoceramic patch actuators *Acoust. Phys.* **52** 398–407

[14] Glushkov E V, Glushkova N V, Kvasha O V and Seemann W 2006 Selective mode excitation in elastic waveguides by piezoceramic actuators *AIP Conf. Proc.* **834** 152–9

[15] Babeshko V A, Glushkov E V and Zinchenko J F 1989 The dynamics of inhomogeneous linearly-elastic bodies *M.: Nauka* (in Russian)

[16] Glushkov E V and Glushkova N V 1997 Blocking property of energy vortices in elastic waveguides *J. Acoust. Soc. Am.* **102** 1356–60

[17] Glushkov E V and Glushkova N V 2001 On the Efficient Implementation of the Integral Equation Method in Elastodynamics *Journal of Computational Acoustics* **9** 889–98

[18] Glushkov E, Glushkova N, Golub M, Boström A 2006 Natural resonance frequencies, wave blocking, and energy localization in an elastic half-space and waveguide with a crack *J. Acoust. Soc. Am.* **119** 3589–98

[19] Aki K, Richards P.G. 1980 Quantitative seismology: Theory and methods: W. H. Freeman and Co., New York

[20] Glushkov E V, Glushkova N V and Kvasha O V 2005 Solution of a dynamic contact problem for an elastic layer with piezoceramic surface-bonded patches *Available from VINITI* No. 1015-B2005 Krasnodar, Kuban State University 1–40 (in Russian)

[21] Seemann W, Ekhlakov A, Glushkov E V, Glushkova N V and Kvasha O V 2006 The modeling of piezoelectrically excited waves in beams and layered substructures *Journal of Sound and Vibration* (to appear)

[22] Wilcox P D, Lowe M J S and Cawley P 2001 Mode and transducer selection for long range wave inspection *J. Intell. Mater. Syst. Struct.* **12** 553–65

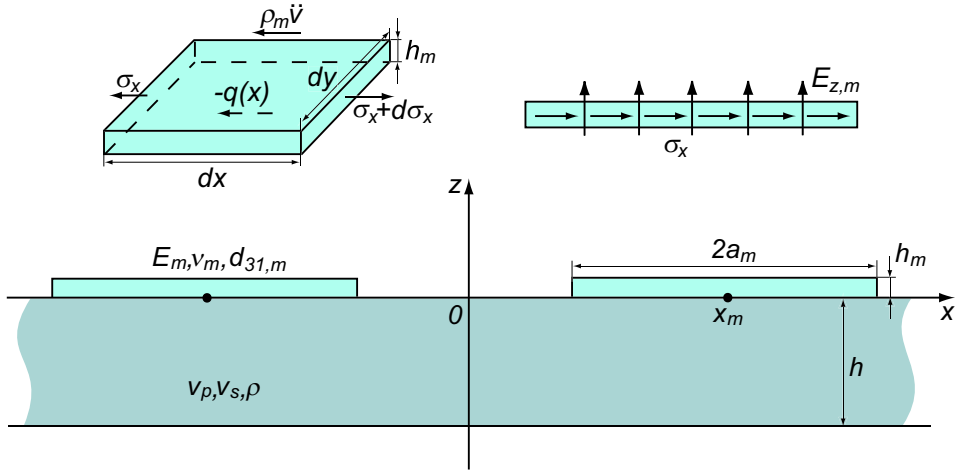

Figure 1. Elastic waveguide with piezoceramic patch actuators.

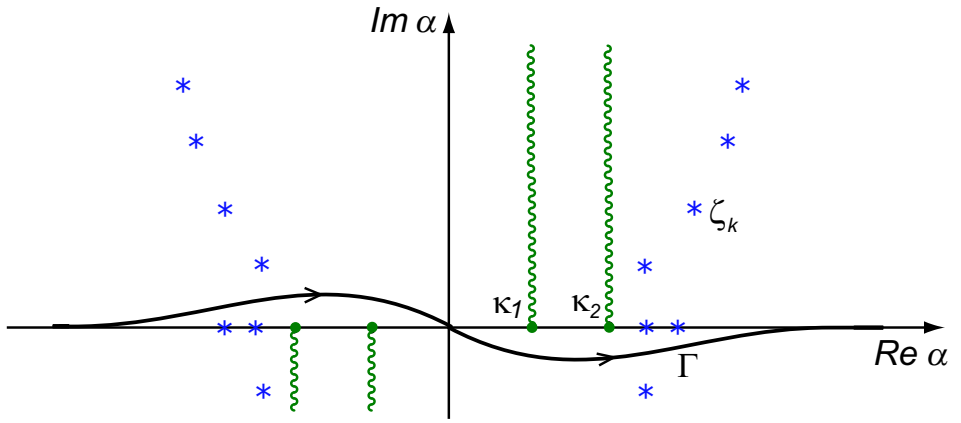

Figure 2. Integration contour Γ, poles ζ_k and cuts in the complex plane α.

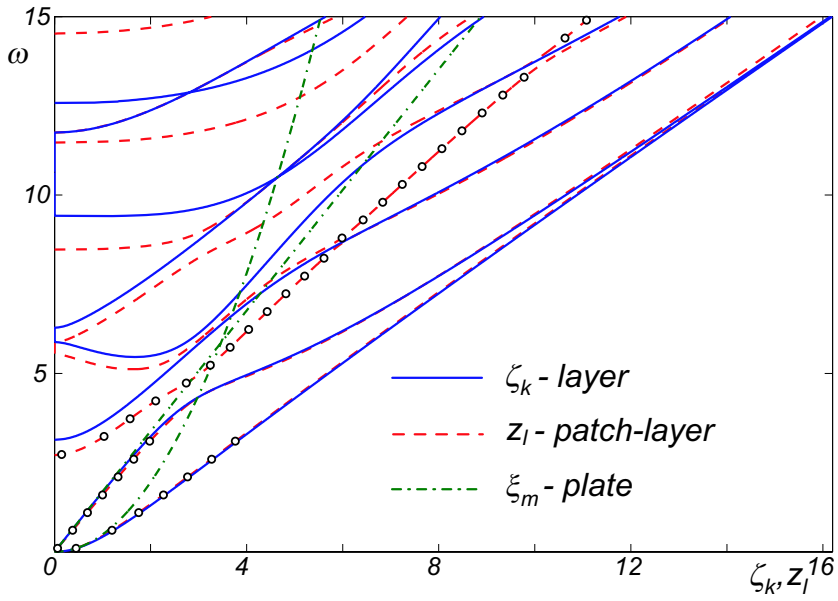

Figure 3. Normal mode wave numbers ζ_k, z_l and ξ_m versus ω (dispersion curves) for elastic layer, patch-layer composite and simplified plate waveguides; the principal patch-layer resonance modes are marked by circles.

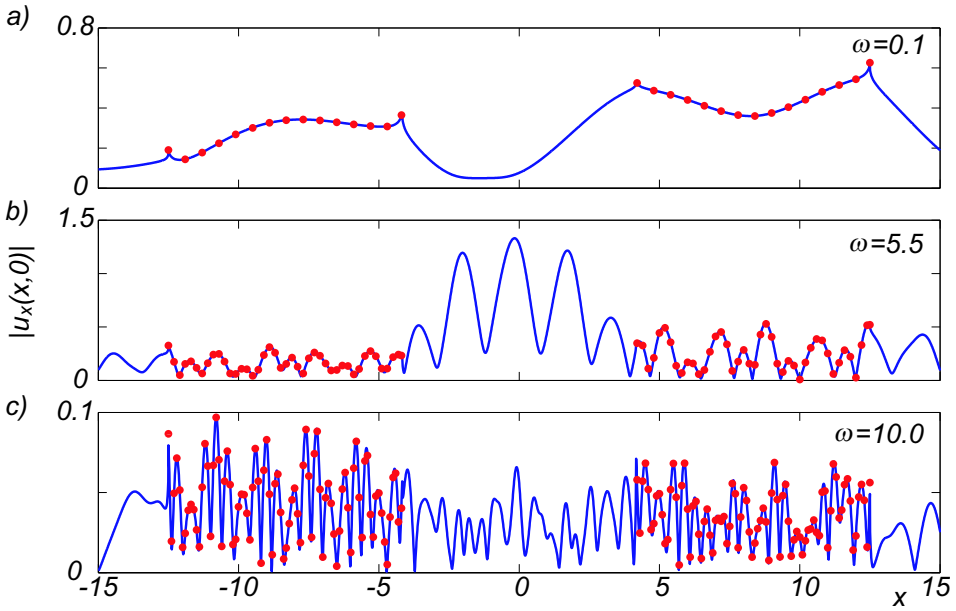

Figure 4. Test of the contact boundary condition (2.8); solid lines and dot markers for $u(x,0)$ and $v(x)$, respectively.

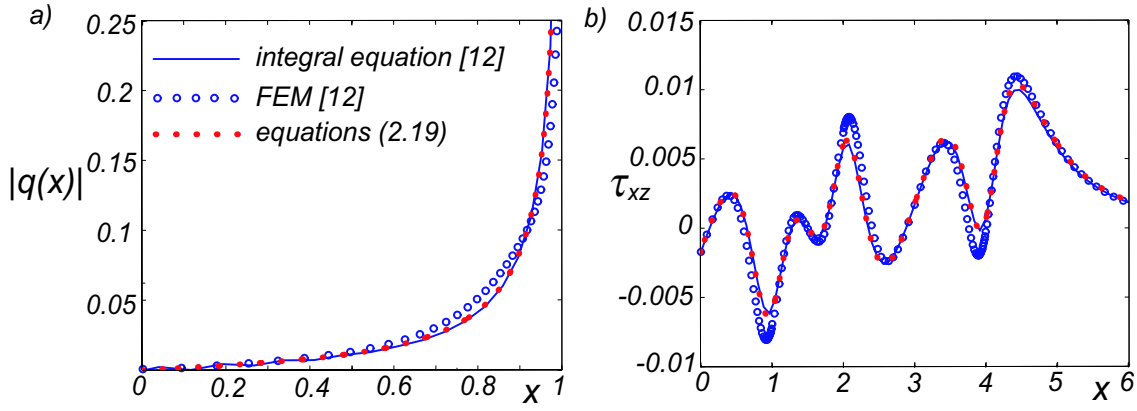

Figure 5. Test comparison versus results from [12] for a half-space substrate; quasistatic contact shear stress distribution $q(x)$ under a single actuator (a) and stress distribution τ_{xz} at the depth $z = -0.5a$ caused by two actuators (b).

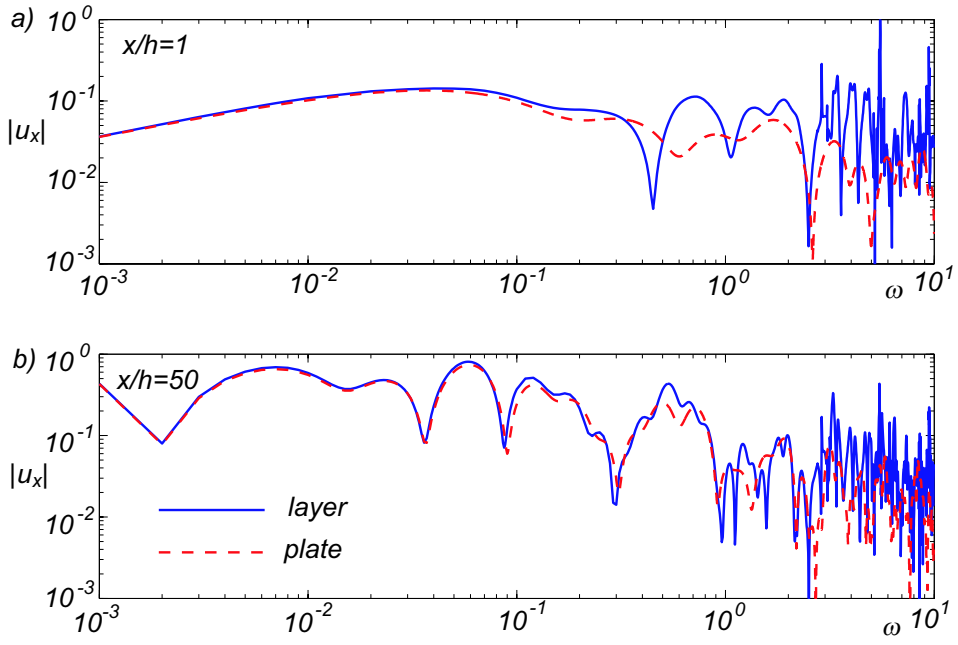

Figure 6. Comparison of the layer and plate models in the frequency domain; surface displacement $|u_x(x,0)|$ versus ω for two points $x = 1$ (between the actuators) and $x = 50$ (far away from them).

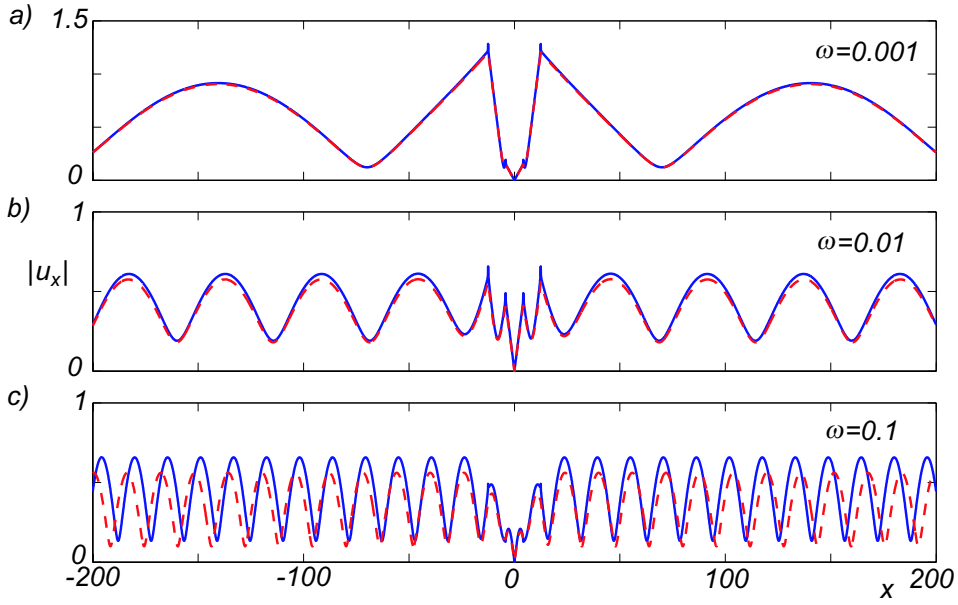

Figure 7. A good agreement of the displacement $|u_x(x,0)|$ spatial distributions provided by the layer (solid lines) and plate (dashed lines) models at low frequencies.

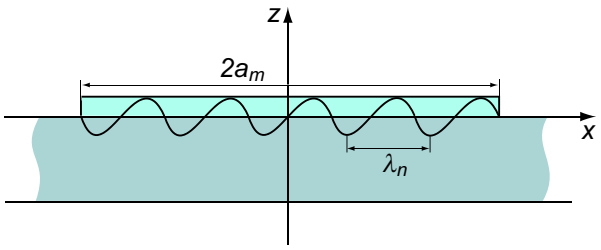

Figure 8. Illustration to the mechanism of strip size resonance.

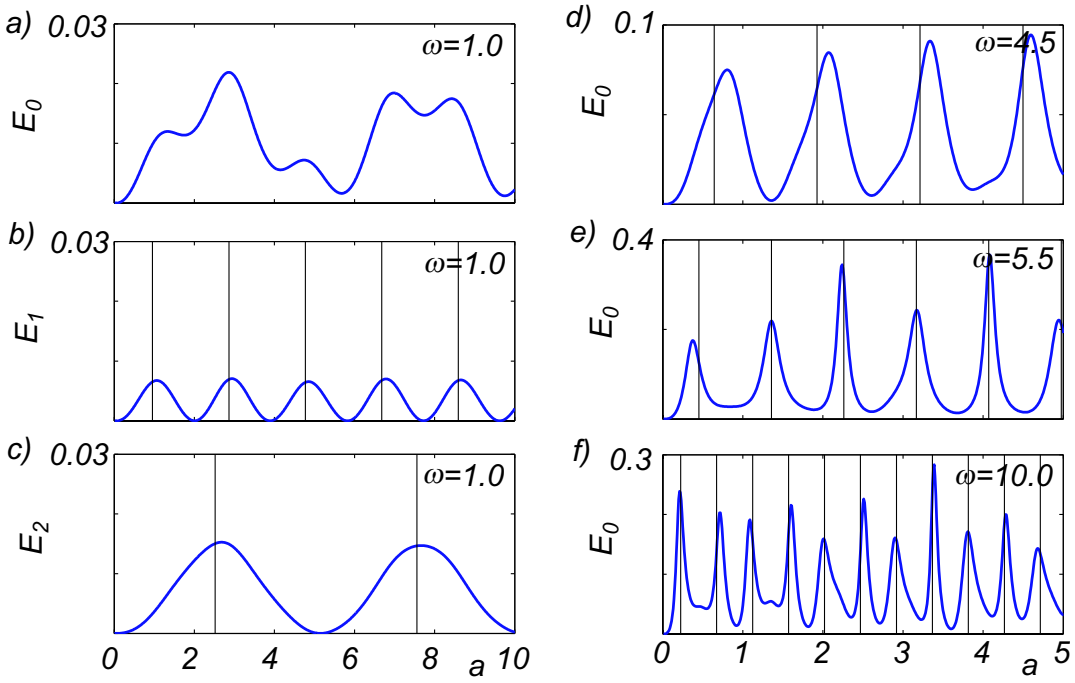

Figure 9. Patch size resonance: radiated energy E_0 versus strip semi-width a; the vertical lines point out the values $a_n = \pi(n + 1/2)/z_l$ for z_l taken from the principal branches marked in figure 3 by circles.

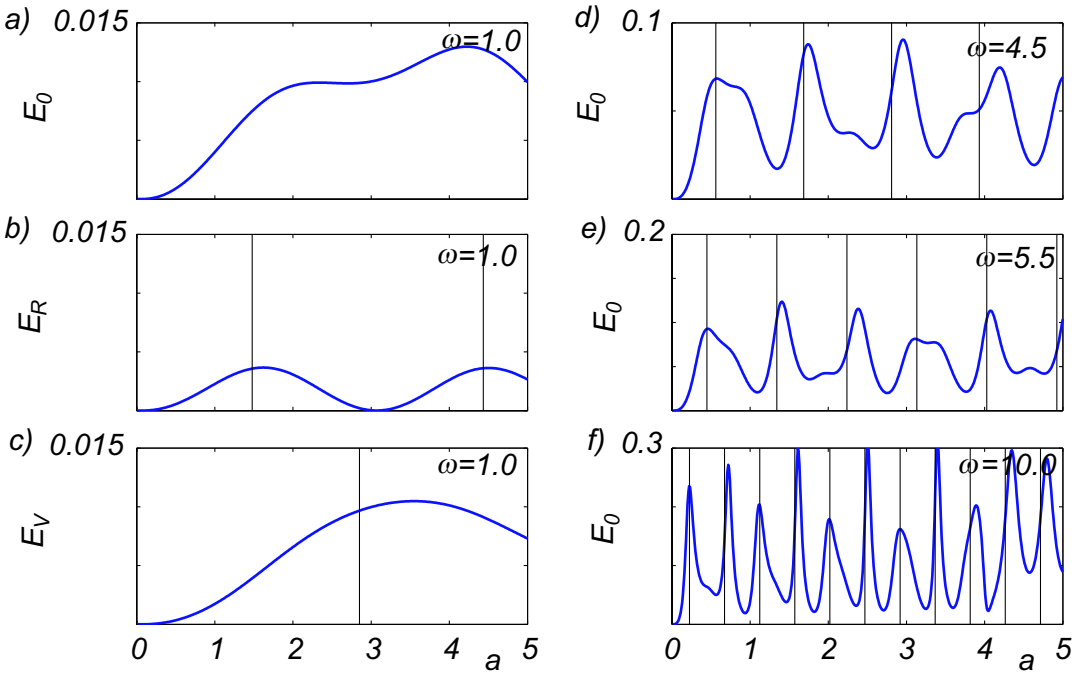

Figure 10. The same as in figure 9 but for a half-plane substrate; in subplots c) - f) $a_n = \pi(n + 1/2)/\mathrm{Re}\, z_2$ where z_2 is given in figure 11.

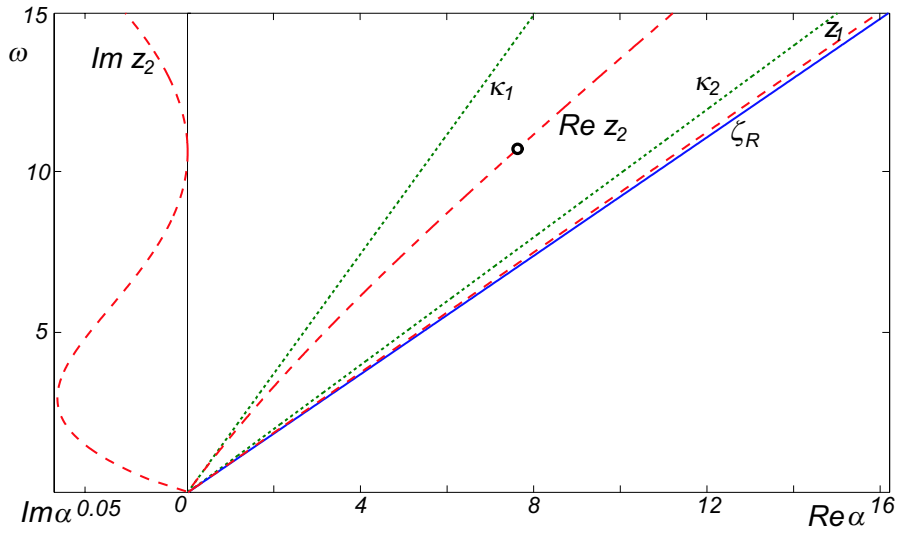

Figure 11. Dispersion curves in the case of half-space host medium; wave numbers of body P and S waves (κ_1 and κ_2), Rayleigh wave (ζ_R) and surface waves of Rayleigh type in the half-space coated by a piezoceramic film (pure real z_1 and complex z_2); the circle is for the pure real value z_2.

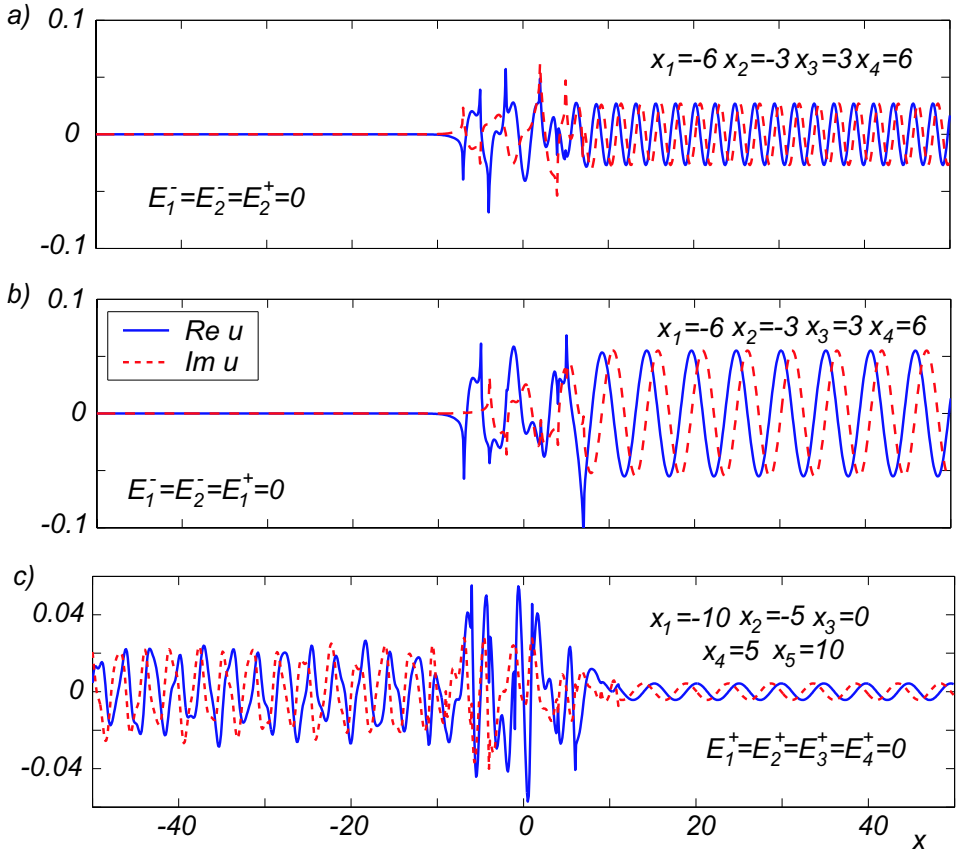

Figure 12. Normal mode selective excitation in a layer: single fundamental modes s_0 and a_0 by four patches at $\omega = 2$ (a) and b)) and selection of the backward mode ζ_5 in the right direction by five patches at $\omega = 5.5$ (subplot c)).

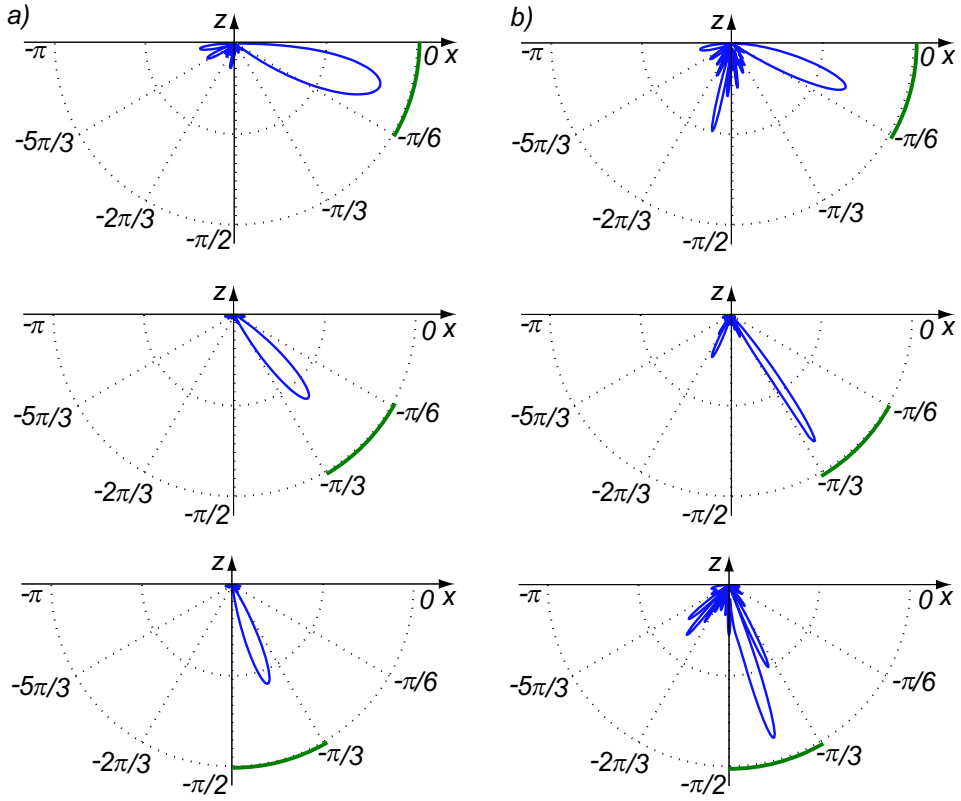

Figure 13. Directional radiation of P and S body waves (left and right subplots a) and b), respectively) in the required angular domains shown by bold arcs.